

Intraseasonal Air–Sea Interaction in the Tropical Indian and Pacific Oceans

HARRY H. HENDON AND JOHN GLICK

CIRES, University of Colorado, Boulder, Boulder, Colorado

(Manuscript received 12 October 1995, in final form 12 August 1996)

ABSTRACT

The relationships between intraseasonal (periods <100 days) variations of convection, sea surface temperature (SST), surface wind stress, and surface fluxes of latent heat and radiation in the warm pool of the equatorial Indian and western Pacific Oceans are examined using 7 yr of gridded outgoing longwave radiation (OLR), SST, and surface stress and latent heat flux based on European Centre for Medium-Range Weather Forecasts analyses. In the warm pool region enhanced evaporation, which results from enhanced surface westerlies, lags enhanced convection by ~ 1 week. Intraseasonal SST fluctuations lag decreased evaporation by ~ 1 week and decreased convection (which implies increased insolation) by ~ 2 weeks, suggesting that anomalous latent heat flux and surface insolation drive SST changes on intraseasonal timescale.

The relationship between anomalous SST, surface wind stress and surface fluxes of latent heat and shortwave radiation for the Madden–Julian oscillation (MJO), which dominates the intraseasonal variability of convection and surface winds over the warm pool, is developed. Spatially coherent SST anomalies, with amplitude of $\sim 1/3^\circ\text{C}$, develop in the Indian Ocean and propagate eastward along with the large-scale convective anomaly, but with 1/4 cycle lag. The SST anomalies in the Indian Ocean are postulated to be driven predominantly by surface insolation anomalies associated with the anomalous large-scale convection. The SST anomalies in the western Pacific are postulated to be driven by a combination of anomalous latent heat flux and insolation. The differing behavior in each ocean reflects structural changes of the MJO as it evolves through its life cycle. Data collected during TOGA COARE are used to quantify the role of surface heat flux anomalies for driving the SST changes in the western Pacific.

1. Introduction

Intraseasonal variability in the tropical troposphere is dominated by the so-called Madden–Julian oscillation (MJO, e.g., Madden and Julian 1972). Its spectral signature in zonal wind and surface pressure is concentrated around 40–50-day period, while that in convection is much broader (i.e., 35–95 days; Salby and Hendon 1994). The dynamical signal of the MJO affects the global Tropics. However, the strongest signal in lower tropospheric wind and convection occurs over the warm pool of the Indian and western Pacific Oceans.

Various composite studies of the MJO have provided insight into the evolution of the large-scale circulation anomalies and their relationship to anomalous convection (e.g., Knutson and Weickmann 1987; Hendon and Salby 1994). Less emphasis has been given to the structure and evolution of the associated surface wind stress and fluxes of latent heat and radiation. Such fluxes are of interest for the mechanism of the MJO (e.g., evaporation–wind feedback, Emanuel 1987) and for inter-

action with the ocean, especially over the warm pool where the signal of convection and surface winds is the strongest. For instance, Zhang and McPhaden (1995) and Zhang (1996) show that at 30–90-d timescales anomalous evaporation leads low SST in the equatorial western Pacific by about 1/4 cycle, suggesting that latent heat flux is important in regulating SST change on this timescale (see also McPhaden and Hayes 1991). Zhang (1996) further speculates that the surface radiative effects of convective cloudiness may also play an important role.

The entire structure of the warm pool mixed layer also changes in response to the intraseasonal variations of surface heat flux and stress. Lukas and Lindstrom (1991) examined the structure of the warm pool mixed layer before and after the passage of a westerly wind event in late January 1986. This wind event was associated with the eastward propagation of a pronounced MJO (e.g., Hsu et al. 1990). Lukas and Lindstrom (1991) showed that the SST dropped more than a degree and the mixed layer deepened from 22 to 44 m after the passage of the wind event. They suggest that anomalous latent heat flux accounted for much of the cooling but that entrainment (as reflected in the deeper mixed layer), driven by wind-generated turbulent energy, also contributed to the cooling.

Corresponding author address: Harry Hendon, CIRES, Campus Box 449, University of Colorado, Boulder, Boulder, CO 80309.
E-mail: hhh@cdc.noaa.gov

Intraseasonal SST variability may also be produced by oceanic Kelvin waves that are forced by intraseasonal variations of zonal stress across the western Pacific warm pool (e.g., Harrison and Schopf 1984; Johnson and McPhaden 1993). Kessler et al. (1995) recently showed that the MJO was primarily responsible for exciting the oceanic Kelvin waves that dominate the intraseasonal variability of the equatorial thermocline in the central and eastern Pacific Ocean. They deduced, in accord with Johnson and McPhaden (1993), that zonal advection of the mean SST field by the anomalous zonal currents associated with these Kelvin waves causes SST anomalies $O(0.5^\circ\text{C})$ eastward of the date line.

The focus of the present study will be on the relationship of intraseasonal variations of surface wind stress and fluxes of latent heat and shortwave radiation with intraseasonal anomalies of convection over the warm pool of the Indian and western Pacific Oceans. The relationship of these fluxes to SST changes on this time- and space scale will be emphasized, as the warm pool is where horizontal gradients of temperature are small and changes in the surface heat flux will presumably dominate SST changes (e.g., Lukas and Lindstrom 1991). The role that the atmospheric MJO plays in these relationships will be explored. Potential feedbacks between the anomalous surface fluxes, atmospheric circulation and convection, and SST will also be explored. The relationship of the MJO with oceanic Kelvin waves and the SST perturbations they cause in the equatorial central and eastern Pacific is the subject of ongoing work, and will be reported later.

2. Data and analysis methods

Continuous records of various oceanic and atmospheric parameters are employed for the 7-yr period July 1986 through June 1993. The principal oceanic dataset is the weekly SST analyses from Reynolds and Smith (1994). The SST analyses cover the entire Indian and Pacific Ocean basins and are available on a 2.5° grid. The principal atmospheric datasets are gridded outgoing longwave radiation (OLR) from National Oceanic and Atmospheric Administration (NOAA's) polar-orbiting satellites and surface fluxes derived from operational analyses at the European Centre for Medium-Range Weather Forecasts (ECMWF). Daily averages of ascending and descending narrowband infrared radiance observations, which are converted to broadband estimates of OLR (Gruber and Krueger 1984), are available on a 2.5° grid. These OLR data are used to infer areas of deep convection. They are also used to infer anomalous surface insolation associated with regions of enhanced convection (section 4).

Daily averaged winds, temperature, mixing ratio, and sea level pressure from ECMWF analyses on a 2.5° grid are used to estimate surface stress and latent heat flux. Bulk aerodynamic approximations are used. The surface stress, $\boldsymbol{\tau} = (\tau_x, \tau_y)$, is estimated as

$$\boldsymbol{\tau} = \rho_A C_d \mathbf{V} |\mathbf{V}|,$$

where $\rho_A = 1.17 \text{ kg m}^{-3}$, $C_d = 1.3 \times 10^{-3}$, \mathbf{V} is the wind vector at 10 m, and $|\mathbf{V}|$ is its magnitude. The latent heat flux, F_{LH} , is estimated as

$$F_{LH} = -\rho_A C_d L |V| \Delta q,$$

where $L = 2.5 \times 10^6 \text{ J kg}^{-1}$, $\Delta q = q_{SST} - q_{1000mb}$, q_{SST} is the saturation mixing ratio at the observed SST (from the Reynolds and Smith analyses) and sea level pressure, and q_{1000mb} is the mixing ratio at 1000 mb. The inclusion of the minus sign in the definition of F_{LH} means that positive anomalies are associated with decreased evaporation and, hence, warming of the ocean. Intraseasonal variations of sensible heat flux are not considered here as they are assumed to be an order of magnitude smaller than those of F_{LH} over the warm pool (e.g., Webster 1994).

The reliability of these estimates of intraseasonally varying stress and latent flux is not known. Especially suspect is the use of a fixed exchange coefficient in the warm pool region where the mean winds are light. Direct measurements of fluxes in this region (e.g., Fairall et al. 1996) suggest that the exchange coefficient increases dramatically at low wind speed ($< 1 \text{ m s}^{-1}$) and, even at zero wind speed, a nonzero latent heat flux is maintained by convective processes. A limited comparison of the fluxes estimated from the ECMWF analyses with those estimated from detailed surface observations during COARE (section 4) suggests that the low wind speed regime is not a serious problem. In fact, good qualitative agreement is found on the intraseasonal timescales of interest here. However, serious discrepancies in magnitude occur during strong westerly wind events when the surface air temperature is close to the SST and the analyzed humidities are lower than measured. Hence, a too strong latent heat flux out of the ocean is estimated by the bulk aerodynamic formula with stability-independent exchange coefficient.

The large-scale structure of intraseasonal variability in the Tropics (e.g., the MJO) is emphasized by averaging all data onto a $5^\circ \text{ lat} \times 10^\circ \text{ long}$ grid for the domain $60^\circ\text{E} - 90^\circ\text{W}$, $30^\circ\text{N} - 30^\circ\text{S}$. As the SST data are available weekly, they are interpolated to daily for compatibility with the other data. To isolate intraseasonal variations, the gridded analyses are filtered (via spectral transform) to periods $30 < \tau < 90$ days. This range of periods captures the broad spectral peaks in atmospheric variability associated with the MJO (e.g., Salby and Hendon 1994) and also that in the SST (section 3; see also Zhang 1996).

Intraseasonal variability associated with the MJO is determined relative to its signature in convection. This signature is objectively determined by EOF analysis of the intraseasonally filtered OLR. The EOF analysis is performed on the covariance matrix for the domain $60^\circ\text{E} - 90^\circ\text{W}$, $15^\circ\text{N} - 15^\circ\text{S}$. Consistent with previous EOF analyses of intraseasonally filtered OLR (e.g., Weick-

mann 1983; Lau and Chan 1985; Murakami et al. 1986), a dominant pair of modes is found that describe a convective disturbance propagating eastward at about 5 m s^{-1} . The mode possesses maximum amplitude localized over the eastern Indian and western Pacific Oceans, where it displays a zonal wavenumber 2 structure. Little amplitude is found east of about 165°W . Associated behavior in other fields is depicted both by composites and by multiple linear regression based on the principal components of the two dominant EOFs (section 3).

In addition to these 7-yr records, observations from the WHOI IMET mooring (Weller and Anderson 1996), deployed at (156°E , 2°S) during TOGA COARE (Webster and Lukas 1992), are examined. These data are available for the Intensive Observing Period (IOP), which ran from 1 November 1992 through 28 February 1993. These data are available hourly, from which daily means were formed. Standard meteorological data were collected, along with net surface shortwave and longwave radiation. A daily estimate of rainfall is provided that combines gauge-measurements on the Research Vessels *Wecoma* and *Moana Wave* and the Atlas mooring just to the south of the IMET mooring (Weller and Anderson 1996). In addition, latent and sensible heat fluxes are available, which are estimates made with the TOGA COARE Bulk Flux Code (Fairall et al. 1996) applied to the surface observations from the IMET mooring.

To quantify the role of surface heat flux anomalies for driving SST changes requires knowledge of the mixed layer depth. Subsurface temperature and salinity from the IMET mooring are used to compute density, which is then used to estimate the mixed layer depth. Temperature data begin at 0.45 m and extend to 45 m with approximately 2-m resolution. Salinity data begin at 2 m and extend to 45 m with approximately 7-m resolution. Between 45 and 124 m salinity and temperature are available with roughly 8-m resolution. Density is computed from these data after they are interpolated onto a vertical grid with 1-m resolution. The mixed layer depth is estimated as that depth at which the density increases by Δd above the surface value. Here, Δd is specified to be equivalent to the density increase produced by a 0.5°C decrease in temperature from the surface value, but with the salinity held constant. Basing the estimates of mixed layer depth on density change rather than temperature change is important in the warm pool, where the large net flux of freshwater contributes significantly to the stratification of the mixed layer. Estimates of the mixed layer depth based on density change are shallower than those based on temperature change alone (e.g., Lukas and Lindstrom 1991).

3. Intraseasonal air–sea interaction

a. SST variance and covariance with OLR and FLH

Prior to examining the relationship between surface wind stress and fluxes of latent heat and shortwave ra-

diation with the large-scale circulation and convective anomalies associated with the MJO, the spectral characteristic of intraseasonal SST variability, and its coherence with OLR and latent heat flux are examined. This is done in order to assess those regions where intraseasonal SST variations are prominent and possibly driven by intraseasonal variations of surface heat flux, particularly those associated with the MJO. It is well known that intraseasonal variations of convection are dominated by the MJO over the equatorial eastern Indian and western Pacific Oceans (e.g., Salby and Hendon 1994). Example spectra of OLR from this region are shown in Fig. 1a for (85°E , Eq.) and in Fig. 1b for (155°E , Eq.). Spectra were computed by Fourier transforming the 7-yr record (1 July 1986–30 June 1993), after removing the first four harmonics of the annual cycle and then tapering the time series with a cosine-rectangular window over the first and last 5%. Raw spectral estimates, with bandwidth 3.9×10^{-4} cycles d^{-1} , were then smoothed with eight passes of a running three-point average, which yields an effective bandwidth of 3.1×10^{-3} cycles d^{-1} (indicated by the horizontal lines in Fig. 1). An indication of the significance of a spectral peak is given by considering the 95% confidence interval for the smoothed spectral estimates at 45 days in Fig. 1a and 43 days in Fig. 1b. Using the technique of Blackman and Tukey (1959) about 55 total degrees of freedom are estimated for the 57 raw frequencies in the band 30–90-d period (note that this is much less than the traditional estimate of 114 degrees of freedom when each spectral estimate is assumed independent). Hence, about 8 degrees of freedom are associated with an individual smoothed spectral estimate in this band. A chi-square test was then used to obtain the indicated 95% confidence limits. The spectra of OLR at these two locations display broad, but significant, spectral peaks between 30 and 90 d.

Also shown in Fig. 1 are spectra of SST. At both locations SST displays a similar broad spectral maximum in the range 30–90 days. Zhang (1996) found a similar spectral peak in the western equatorial Pacific using three years of area-averaged (8°N – 8°S , 147° – 170°E) buoy data. Examination of the 95% confidence intervals in Fig. 1 suggests, however, that the signal is not as prominent in SST as in OLR.

Those regions where intraseasonal SST fluctuations are relatively prominent are indicated by considering the distribution of the ratio of 30–90-d variance to the total subseasonal (periods less than 200 d) variance (Fig. 2). Broad regions of greater than 50% of the subseasonal variance cover the equatorial Indian and western Pacific Ocean (see also Krishnamurti et al. 1988). The location and extent of the regions with greater than 50% of the subseasonal variance are similar to those where a significant intraseasonal spectral peak in OLR is found (e.g., Salby and Hendon 1994).

The relationships of these intraseasonal SST variations with fluctuations in latent heat flux are considered

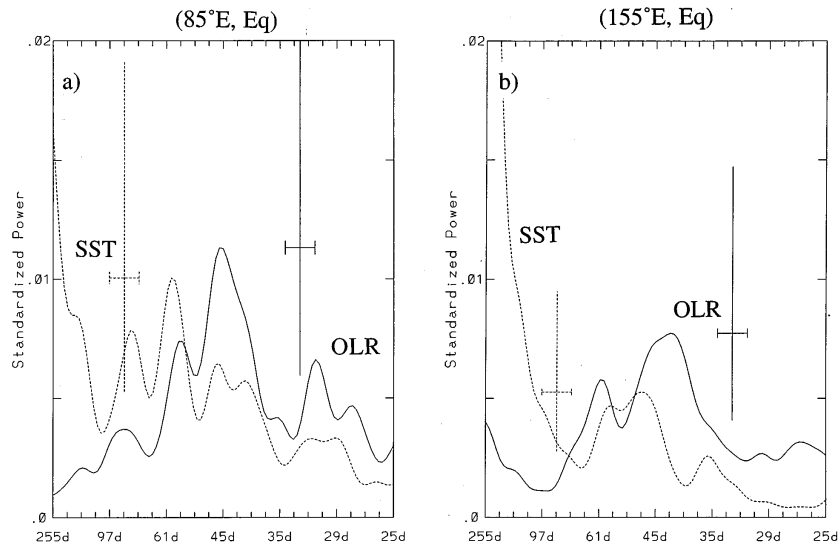


FIG. 1. Power spectra of OLR (solid line) and SST (dotted line) for (a) the grid box centered at (85°E, Eq.) and (b) the grid box centered at (155°E, Eq.). Spectra were normalized by their respective total powers. Spectra were computed using the 7-yr record 1 July 1986–30 June 1993. The seasonal cycle was removed prior to computing the power via spectral transform. Horizontal bars indicate bandwidth for the smoothed spectral estimates. Vertical bars indicate the 95% confidence limits for the spectral estimates at 45-d period (OLR) and 60-d period (SST) in (a) and at 43-d period (OLR) and 49-d period (SST) in (b).

by forming lagged correlations via inverse transform of the cross power in the 30–90-d band. Cross correlations are computed over all pairs of time series for the Indian Ocean (60°–100°E, 15°N–15°S; Fig. 3a) and the western Pacific (150°–180°E, 15°N–15°S; Fig. 3b). In both domains anomalous latent heat flux (reduced evaporation) leads SST by ~ 1 week. Peak correlations are about 0.4. Conservatively assuming that none of the grid boxes in each domain is independent and that there are 55 degrees of freedom in the 30–90-d band (see above), a correlation of 0.2 is significant at the 95% level. Zhang and McPhaden (1995) found correlations with similar magnitude but slightly greater lag (10 days) using surface data from moorings in the western Pacific. They interpret this lag as indicative that latent heat flux is driving SST changes on this timescale (see also McPhaden and

Hayes 1991). The slight difference in lag found here may result from the use of weekly averaged SST data. Nonetheless, the present results are broadly similar to those of Zhang and McPhaden (1995) and thus provide some confidence that similar physics is captured in the latent heat flux based on the ECMWF analyses.

Also shown in Fig. 3 are the cross correlations between OLR and SST. In both basins the peak correlation is about 0.5 with SST lagging OLR by ~ 2 weeks, which is about a quarter cycle for a 50-d period. If the OLR fluctuations on these timescales are indicative of fluctuations of shortwave radiation reaching the surface as a result of albedo changes due to fluctuations in convection, then this lag suggests that fluctuations of surface insolation are also driving SST changes on these timescales. Zhang (1996), who used a similar 30–90-d

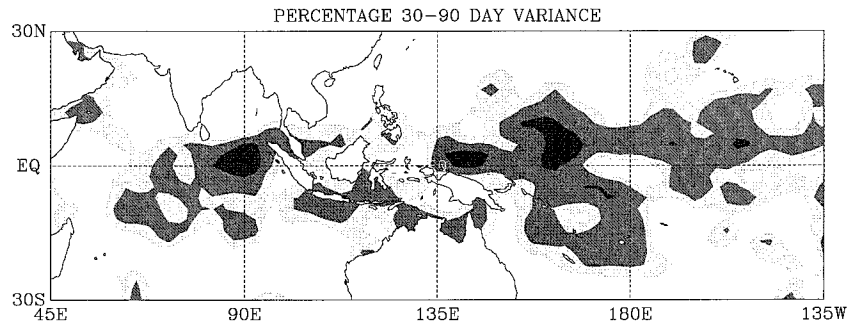


FIG. 2. Ratio (percentage) of intraseasonal (30–90-d period) SST variance to the total subseasonal (periods <200 d) SST variance for the period 1 July 1986–30 June 1993. Shading levels begin at 45%, 50%, and 60%.

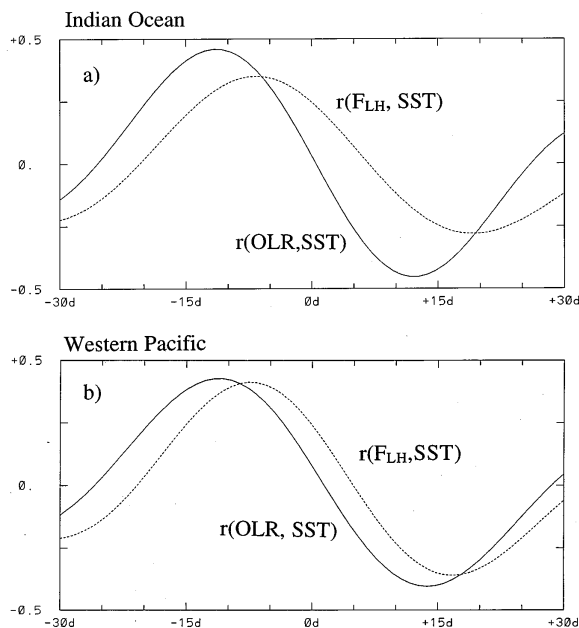


FIG. 3. Lag-correlation of intraseasonally filtered (30–90-d period) SST with OLR (solid lines) and SST with latent heat flux (dotted line). The correlations were computed for all pairs of time series in the domain (a) 60° – 100° E, 15° S– 15° N, and (b) 150° – 180° E, 15° S– 15° N. Negative lag means that OLR and latent heat flux lead SST. Correlations of 0.2 are significant at the 95% level.

band with buoy data in the western equatorial Pacific, finds a stronger correlation (~ 0.7) between SST and high cloudiness (derived from OLR). He also finds a smaller lag, with warm SST lagging decreased high cloudiness by about ~ 0.1 cycle (about 5 d). Possible reasons for these discrepancies are discussed in section 5.

The differing lags between OLR and latent heat flux with SST may indicate that either or both fluxes are important for driving SST changes but that a systematic relationship between OLR and latent heat flux exists on the intraseasonal timescale. This is explored by examining the correlation between OLR and latent flux (Fig. 4). Indeed, in both basins OLR leads the latent heat flux by 1–2 weeks: maximum evaporation from the ocean surface occurs some 1–2 weeks after maximum convective activity. As will be shown below, and in agreement with Zhang and McPhaden (1995) and Zhang (1996), fluctuations of latent heat flux on these timescales over the warm pool are primarily driven by wind-speed variations. The lag between OLR and latent heat flux is consistent with previous observations of the MJO, whereby anomalous surface westerlies (positive windspeed anomaly in these two regions) lag maximum convection by up to 2 weeks (Hendon and Salby 1994). The lag between latent heat flux and OLR is about 2 weeks in the Indian Ocean but less than 1 week in the western Pacific. This feature is also consistent with the tendency for the convective anomaly associated with the MJO to shift from near the node of the surface zonal wind when it is over the Indian Ocean into the surface

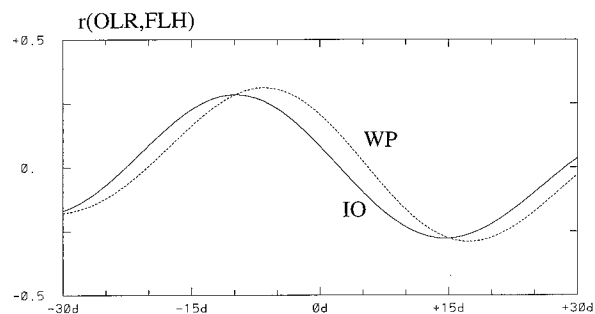


FIG. 4. Lag-correlation of intraseasonally filtered (30–90-d period) latent heat flux with OLR for all grid points in the domain 60° – 100° E, 15° S– 15° N (solid line), and 150° – 180° E, 15° S– 15° N (dotted line). A negative lag means that OLR leads latent heat flux. Correlations of 0.2 are significant at the 95% level.

westerlies when it is over the western Pacific (Hendon and Salby 1994; their Fig. 9c). The implication of this changing phase for the response in SST will be discussed below.

b. Composite analysis based on EOFs of OLR

The relationship of intraseasonal variations of SST, surface wind stress, and fluxes of latent heat and short-wave radiation associated with the MJO is now explicitly addressed. This will be done relative to the convective signature of the MJO as revealed by EOF analysis of OLR. Figure 5 displays the first 10 eigenvalues from the EOF analysis of intraseasonally filtered OLR, along with estimates of their sampling error (North et al. 1982). In computing the sampling errors, 55 degrees of freedom were assumed (see above). The first two eigenvalues are not distinguishable from each other but they clearly stand out from the next eight. The principal components of these two eigenmodes are predominantly in quadrature at near 50-d period (not shown). These two eigenmodes thus describe a spatially propagating phenomenon (see below), which is taken here to be the convective signature of the MJO (see also Weickmann 1983; Lau and Chan 1985; Murakami et al. 1986).

The first two eigenmodes account for about 34% of the intraseasonal OLR variance over the domain 60° E– 90° W, 15° N– 15° S. The variance of SST, τ_x , and F_{LH} accounted for by these two eigenmodes is estimated as follows: At each grid point, these fields are reconstructed by multiple linear regression onto the leading two principal components. The square of the correlation coefficient, computed over all grid points, between these reconstructed fields and their respective input fields yields the explained variance (e.g., Panofsky and Briar 1968). To provide insight into the seasonal and interannual variation of the explained variance, these explained variances, along with that for OLR, are calculated within a moving 140-d moving window (Fig. 6). All fields exhibit a distinct seasonal variation of explained variance, though interannual variations are

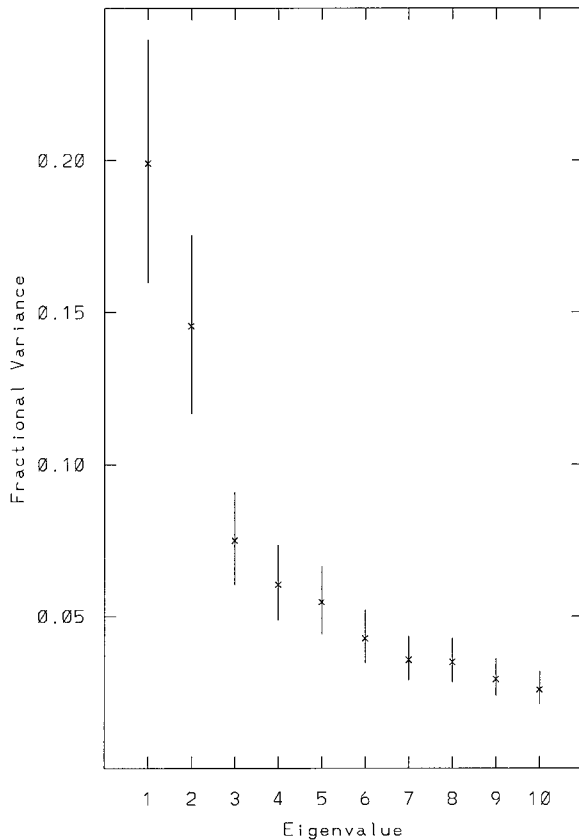


FIG. 5. The first 10 eigenvalues from the EOF analysis of intraseasonally filtered (30–90 d) OLR on the domain 60°E–90°W, 15°N–15°S. The eigenvalues are scaled such to indicate the fractional variance of the input field accounted for by each EOF. Vertical bars are estimates of sampling errors as given by North et al. (1982).

prominent as well. Peak values approach twice the mean amounts from about October through March, while minimum explained variance tends to occur during May through August. This seasonal variation is in accord with previous studies of the seasonal cycle of the MJO (e.g., Salby and Hendon 1994).

Insight into the geographical distribution of the signal of the MJO in each field is provided by computing the explained variances for those times when the explained variance for OLR exceeds its mean value of 34% (as given by the sum of the two eigenvalues, Fig. 5). Figure 7 displays the explained variances averaged over 15°N–15°S, as a function of longitude, for OLR, τ_x , F_{LH} , and SST. Maxima occur over the Indian and western Pacific Oceans. Peak values for OLR exceed 50%, which is consistent with previous estimates of the strength of the convective signal of the MJO during boreal winter through early spring (e.g., Salby and Hendon 1994). Only τ_x exhibits a local maxima in the eastern Pacific. Large explained variance in the other fields is confined to the region where the convective signal is strong and where the circulation anomalies associated with the MJO are coupled to the convective anomalies (Salby

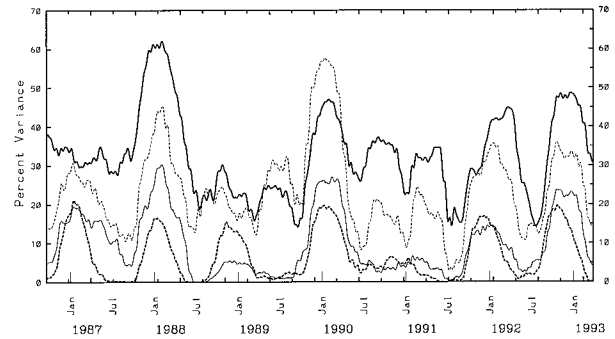


FIG. 6. Variance explained of OLR (heavy solid line), zonal stress (light dotted line), latent heat flux (thin solid line), and SST (dashed line) by the leading two eigenmodes from the OLR-based EOF analysis. The explained variances were computed within a moving 140-day window over the domain 60°E–90°W, 15°N–15°S for the period 1 July 1986–30 June 1993.

and Hendon 1994). The local maxima for τ_x in the eastern Pacific reflects the contribution by the radiating disturbance in the zonal wind, which emanates from near the dateline as the convective anomaly collapses (Madden and Julian 1972; Hendon and Salby 1994; Hendon and Salby 1996).

The spatial structure of the OLR anomalies and their relationship to the associated atmospheric fluxes and SST anomalies are depicted by forming composites based on the principal components of the two leading EOFs. Four main categories (i.e., 1, 3, 5, and 7) are specified according to when maxima and minima of each principal component exceed ± 1.5 standard deviation. About 16 events fall into each category. Because the dominant period of the mode depicted by the two EOFs is about 50 days, the temporal spacing between each main category is about 12 days.

Figure 8a displays the composite anomalies of OLR (shaded), SST (contoured), and stress (vectors) for category 1 (maximum of principal component 1). Figure 8b displays anomalies of the same fields for category 3 (maximum of principal component 2), which is 1/4

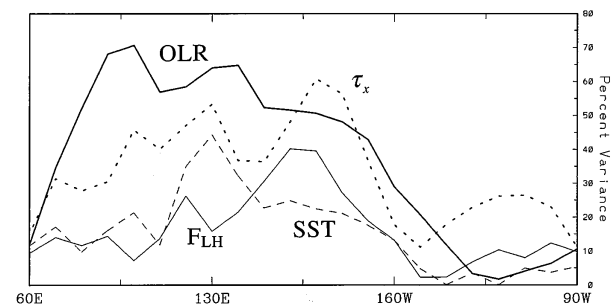


FIG. 7. Variance explained of OLR (heavy solid), zonal stress (dotted), SST (dashed), and latent heat flux (dotted) by the leading two eigenmodes from the OLR-based EOF analysis for the domain 15°N–15°S as a function of longitude. The explained variances were computed for those periods when the domain-averaged explained variance for OLR (Fig. 6) exceeded its mean amount of 34%.

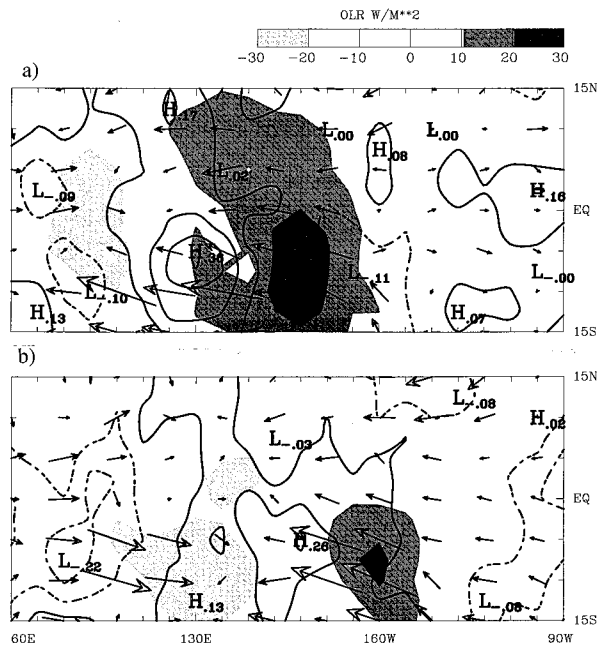


FIG. 8. Composites of intraseasonal anomalies of OLR (shaded, $W m^{-2}$), SST ($0.1^{\circ}C$ contour interval with first contour at $\pm 0.05^{\circ}C$), surface stress (maximum vector $0.04 N m^{-2}$) for times when the magnitude of the principal component of (a) eigenmode 1 and (b) eigenmode 2 from the OLR-based EOF analysis exceed 1.5 standard deviations. Panel (a) leads panel (b) by about 1/4 cycle, or roughly 2 weeks.

cycle later. The structures for category 5 (minimum of principal component 1) and 7 (minimum of principal component 2) are nearly identical to those for category 1 and 3 but with opposite sign (not shown).

OLR and surface stress exhibit characteristics typical of the life cycle of the MJO during boreal winter and early spring (e.g., Hendon and Salby 1994), the season to which the EOF analysis discriminates (cf. Fig. 6): The OLR signal is confined to the equatorial Indian and western Pacific Oceans, where it exhibits a zonal wavenumber 2 structure. The OLR anomalies are displaced into the Southern Hemisphere especially in the western Pacific, where climatological convection is displaced south of the equator during boreal winter. Westerly stress extends about two-thirds of the way across the region of enhanced convection in the Indian Ocean. On the other hand, westerly stress extends completely across the region of enhanced convection in the western Pacific (as inferred from anomalies of opposite sign in Fig. 8).

SST anomalies display largest amplitude around $5^{\circ}S$ and west of about $160^{\circ}W$, the region to which OLR displays largest amplitude. SST anomalies are locally in quadrature with the OLR anomalies, in agreement with the cross-correlation analyses (Fig. 3). The amplitude of the SST anomalies is about $1/4^{\circ}$ – $1/3^{\circ}C$, which is consistent with analyses from moorings in the equatorial western Pacific (Zhang and McPhaden 1995; Zhang 1996).

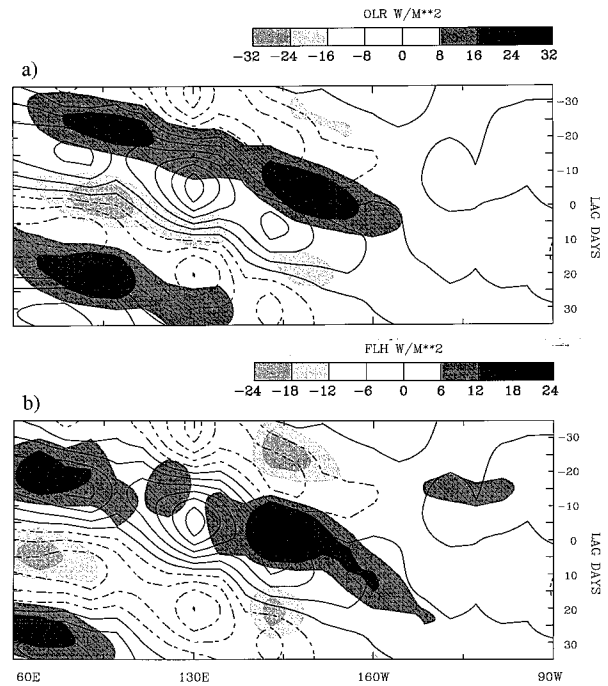


FIG. 9. Hovmöller representation along $5^{\circ}S$ of the lagged-regression of (a) OLR ($W m^{-2}$, shaded) and SST (contoured), and (b) latent heat flux ($W m^{-2}$, shaded) and SST (contoured) onto the two leading principal components of the EOFs of OLR. Anomalies are scaled for a 1.5 standard deviation of the principal components. The contour interval for SST is $0.05^{\circ}C$.

To emphasize the temporal evolution and eastward propagation of the convective anomaly and associated SST and surface flux anomalies, lagged regression of intraseasonally filtered fields onto the two leading principal components are formed. The regressions are scaled for a 1.5 standard deviation of each principal component. These regressions are displayed as lagged-Hovmöller maps centered at $5^{\circ}S$ (the latitude where the SST anomalies are largest). Figure 9a displays the lagged regression of OLR (shaded) and SST (contoured). Both fields exhibit eastward propagation at $\sim 5 m s^{-1}$ across the Indian and western Pacific, which is characteristic of the MJO across this region. Cold SST follows enhanced convection by about 1/4 cycle (~ 2 weeks). This quadrature relationship is maintained across the Indian Ocean to the western Pacific. Figure 9b displays the lagged regression of F_{LH} (shaded) and SST (contoured). Recall that positive anomalies of F_{LH} are associated with decreased evaporation and, hence, imply warming of the ocean. Here, F_{LH} anomalies are also seen to propagate systematically eastward and to display little amplitude east of about $160^{\circ}W$. The F_{LH} anomalies lead the SST anomalies by about 1 week across the Indian Ocean and by about 2 weeks across the western Pacific. The change in phase of F_{LH} relative to the SST anomalies reflects that the phase is also changing relative to OLR, such that the OLR anomalies lead the F_{LH} anomalies by

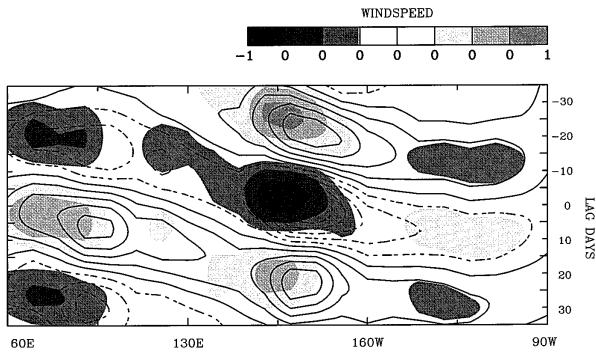


FIG. 10. Hovmöller representation along 5°S of the lagged-regression of surface wind speed (m s^{-1} , shaded) and zonal stress (contoured), onto the two leading principal components of the EOFs of OLR. Anomalies are scaled for a 1.5 standard deviation of the principal components. The contour interval for zonal stress $5 \times 10^{-3} \text{ N m}^{-2}$.

a greater amount in the Indian Ocean than in the western Pacific. This change in phase between the OLR and F_{LH} anomalies in each basin is consistent with the phase change depicted by cross correlation analysis of intraseasonally filtered data (Fig. 3c).

The correspondence of the F_{LH} anomalies with wind-speed perturbations is confirmed by considering the lagged regression of the windspeed anomalies (Fig. 10). Also shown in Fig. 10 are the regressed τ_x anomalies. The structure of the τ_x anomalies is indicative of the life cycle of surface zonal wind for the MJO (e.g., Hendon and Salby 1994): eastward propagation at about 5 m s^{-1} occurs across the Indian and western Pacific while east of about 160°W , where the convective anomaly is diminished, much more rapid propagation occurs ($10\text{--}20 \text{ m s}^{-1}$) associated with the radiating disturbance (e.g., Hendon and Salby 1994, 1996). Across the Indian and western Pacific Oceans, where weak mean westerlies prevail during much of the year and particularly in boreal winter and early spring, westerly stress anomalies correspond to positive windspeed anomalies and enhanced evaporation. East of about 160°W , where easterly trades prevail, the opposite is true. Note, however, that latent heat flux anomalies are essentially absent there. By comparing to Fig. 8a, it is again apparent that surface westerlies lag enhanced convection by less than 1 week in the western Pacific but lag enhanced convection by about ~ 2 week in the Indian Ocean.

The interrelationships between the various fields and fluxes are examined further for a grid box in the Indian Ocean (Fig. 11a) and in the western Pacific (Fig. 12a). Here, F_{LH} leads SST by less than 1 week in the Indian Ocean and by about 2 weeks in the western Pacific, while SST is nearly in quadrature with OLR in both locations. This quadrature relationship between OLR and SST in both basins, despite the more in-phase relationship between F_{LH} and SST in the Indian Ocean, may indicate that insolation anomalies are relatively more important than F_{LH} anomalies for driving SST

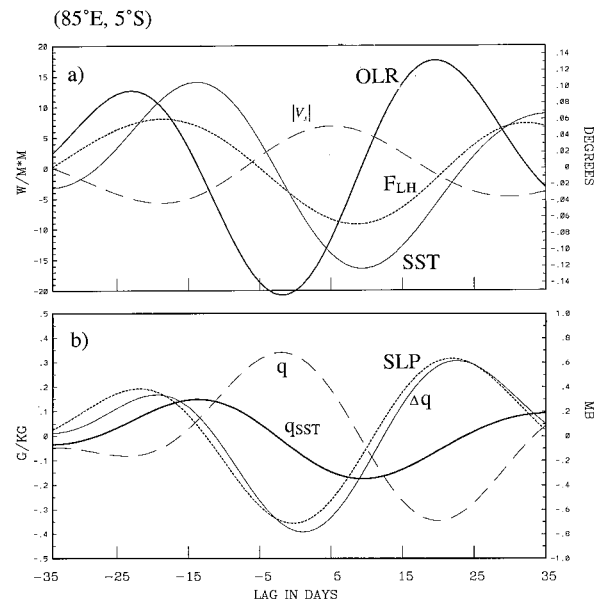


FIG. 11. (a) Time series at $(85^{\circ}\text{E}, 5^{\circ}\text{S})$ of lagged-regression of anomalous OLR (heavy solid line), SST (light solid line), latent heat flux (dotted line), and surface wind speed (dashed line) onto the leading two principal components of the OLR-based EOF analysis. Anomalies are scaled for a 1.5 standard deviation of the principal components. The scale for OLR and latent heat flux (W m^{-2}) is on left ordinate. The scale for SST ($^{\circ}\text{C}$) is on right ordinate. The scale for wind speed is on left ordinate in units of 10 m s^{-1} (that is, the amplitude of the wind speed fluctuation is about 0.5 m s^{-1}). (b) As in (a) except for anomalous q (dashed line), q_{sst} (heavy solid line), Δq (light solid line), and sea level pressure (dotted line). The scale for q , q_{sst} , and Δq is on the left ordinate (g kg^{-1}). The scale for sea level pressure is on the right ordinate (mb).

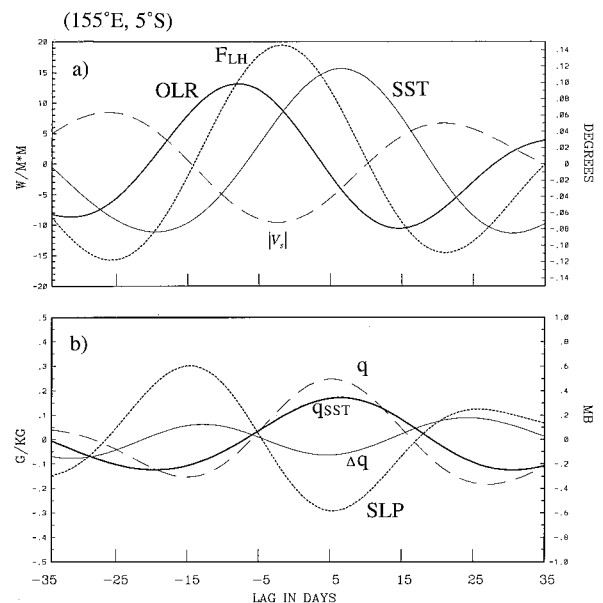


FIG. 12. As in Fig. 11 except at $(155^{\circ}\text{E}, 5^{\circ}\text{S})$.

changes in the Indian Ocean. Consistent with this premise is the observation that the relative amplitude of the OLR anomaly as compared to the F_{LH} anomaly is larger in the Indian Ocean.

In both basins (Figs. 11a and 12a) F_{LH} anomalies vary inversely with wind speed. However, a slight lag of about 5 days between the maximum wind speed and minimum F_{LH} (maximum evaporation) is detectable in the Indian Ocean. This lag probably results from the greater amplitude and lag with wind speed of Δq in the Indian Ocean (Fig. 11b) than in the western Pacific (Fig. 12b). Again, these differences are consistent with the observed structural changes of the MJO over its life cycle. In both basins, Δq is primarily determined by changes in atmospheric q . Fluctuations in q appear not to be determined by local evaporation, as q is observed to lead the evaporation by 1–2 weeks in each basin. Rather, q is more likely determined by low-level convergence. Hendon and Salby (1994) show that the near-equatorial surface convergence, whereby cross-isobaric meridional flow converges into the surface low, is nearly in phase with the convective anomaly while it is developing in the Indian Ocean. This is reflected here by the small phase lag between q and negative anomalies of OLR and surface pressure (Fig. 11). As the MJO evolves and propagates eastward, Hendon and Salby (1994) show the lag between the convective anomaly and surface convergence (and surface low pressure) increases to about 1/4 cycle (~ 2 weeks). A similar lag is observed here between anomalous q and the negative anomalies of surface pressure and OLR (Fig. 12). On the other hand, Zhang (1996) shows the q anomaly to be in phase with anomalous high cloudiness over the equatorial western Pacific. He further shows the evaporation anomaly to be nearly in phase with the cloudiness anomaly. Again, these important discrepancies, possibly associated with the averaging of unequally distributed buoy data by Zhang (1996), are addressed in section 5.

The lesser amplitude of Δq in the western Pacific also stems from the relative phasing of the SST and q anomalies. In the western Pacific they are all in phase, so that Δq results from the small difference of q and the saturated value at the SST. In the Indian Ocean, where the q anomaly is more in phase with the convective anomaly and in quadrature with the SST anomaly, Δq is larger because of less cancellation by the fluctuation of the saturated value at the surface.

In summary, on intraseasonal timescales enhanced evaporation lags enhanced convection by 1–2 weeks. Across the Indian and western Pacific, where the latent heat flux anomalies associated with the MJO are confined, enhanced evaporation stems from enhanced surface westerlies. Over the life cycle of the MJO, anomalous evaporation shifts from lagging anomalous OLR by about 1/4 cycle (~ 2 weeks) across the Indian Ocean to less than 1 week across the western Pacific. This change in phasing is consistent with previous obser-

vations that show the convective anomaly to evolve from near the node of the surface zonal wind over the Indian Ocean into the surface westerlies across the western Pacific (e.g., Hendon and Salby 1994). Similarly, anomalous surface moisture, presumably driven by surface convergence, evolves from being in phase with the convective anomaly over the Indian Ocean to leading it by 1/4 cycle in the western Pacific. Spatially coherent SST anomalies accompany the eastward propagating OLR anomalies associated with the MJO, but with about a 1/4 cycle lag. These SST anomalies are postulated to be driven predominantly by anomalous insolation in the Indian Ocean and by a combination of anomalous latent heat flux and insolation in the western Pacific.

4. Intraseasonal air–sea interaction during COARE

Observations taken during TOGA COARE are used to quantify the role of MJO-induced anomalies of insolation and latent heat flux for generating SST anomalies in the Indian and western Pacific Oceans. The quality of the stress and latent heat flux estimates based on the ECMWF analyses will also be accessed. Three intraseasonal fluctuations of convection traversed the Intensive Flux Array (IFA, roughly 2°N – 2°S , 152° – 157°E) between October 1992 and February 1993 (Gutzler et al. 1994). The three events crossed the IFA at the end of October, the end of December, and the end of January. As the IOP ran from 1 November 1992, the late October event was not as well sampled as the succeeding two events. SST anomalies of order 0.5°C in the Indian and western Pacific Oceans accompanied the eastward migrating convective events (Gutzler et al. 1994).

The variability observed during the IOP, which can be attributed to the MJO, is gauged by examining reconstructed anomalies of SST and OLR for October 1992 through April 1993 (Fig. 13). These reconstructed anomalies were generated by multiple linear regression onto the principal components of the two leading EOFs of intraseasonally filtered OLR. Note that maxima in each of the explained variances by these reconstructed fields occurred during the IOP (Fig. 6). The most prominent intraseasonal convective variation that traversed the IFA is the enhanced-suppressed-enhanced episode during December through early February, which was associated with eastward propagating anomalies originating in the Indian Ocean. The strongest intraseasonal SST anomalies, which track the OLR anomalies across the Indian and western Pacific Oceans, occur at this time as well.

The first issue to address is the reliability of the fluxes estimated from the ECMWF analyses. Surface stress and latent heat flux for the grid box centered at (155°E , 2.5°S) are compared to those estimated from the IMET mooring (Weller and Anderson 1996) for 1 November 1992 through 28 February 1993. A weekly average was applied to both fluxes in order to emphasize intrasea-

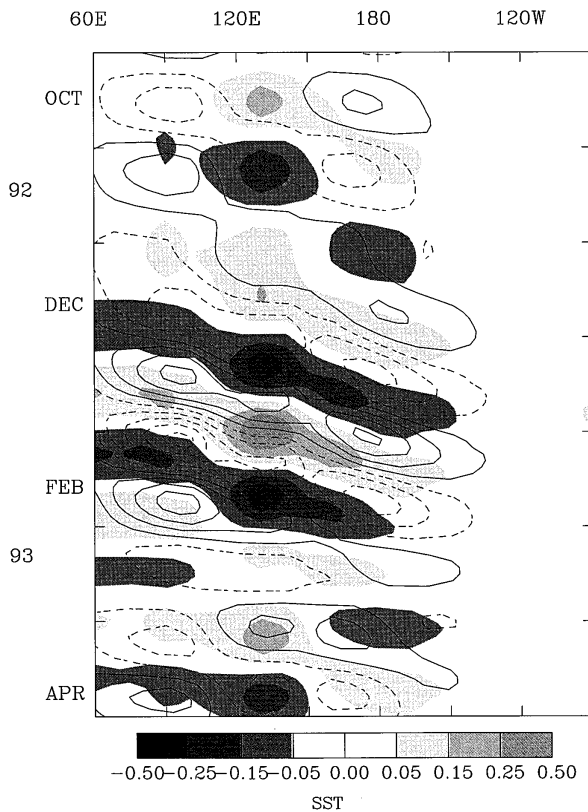


FIG. 13. Hovmöller map along 5°S of anomalies of OLR (contoured, contour interval 10 W m^{-2}) and SST (shaded, $^{\circ}\text{C}$) reconstructed from the leading 2 eigenmodes of intraseasonally filtered OLR. The period 1 October 1992 through 15 April 1993 is shown.

sonal timescales. The time series of $|\tau|$ is shown in Fig. 14a. The mean stress for this period, estimated from the EC analyses, is $3.0 \times 10^{-2} \text{ N m}^{-2}$, while the IMET estimate is slightly larger ($3.5 \times 10^{-2} \text{ N m}^{-2}$). Similar temporal variability is displayed in each estimate as reflected by their comparable standard deviations ($2.2 \times 10^{-2} \text{ N m}^{-2}$ for the ECMWF estimate and 2.1×10^{-2} for the IMET estimate) and by their correlation coefficient of 0.84. Their root-mean-square difference is $1.2 \times 10^{-2} \text{ N m}^{-2}$. The large (westerly) stress events accompanying the enhanced convective activity in late December and early February (Fig. 13), in particular, are well captured in the ECMWF-based estimate. However, a systematic deficiency exists in late November through early December. Overall, the agreement between the two estimates of surface stress is probably as good as can be expected for a point-to-grid box comparison.

The two estimates of latent heat flux are displayed in Fig. 14b. The mean latent heat flux is -122 W m^{-2} from the ECMWF-based estimate and is -106 W m^{-2} from the IMET estimate. The more negative flux (larger evaporation) from the ECMWF estimate results largely from enormous evaporation during the two large wind events. The favorable comparison of the magnitude of

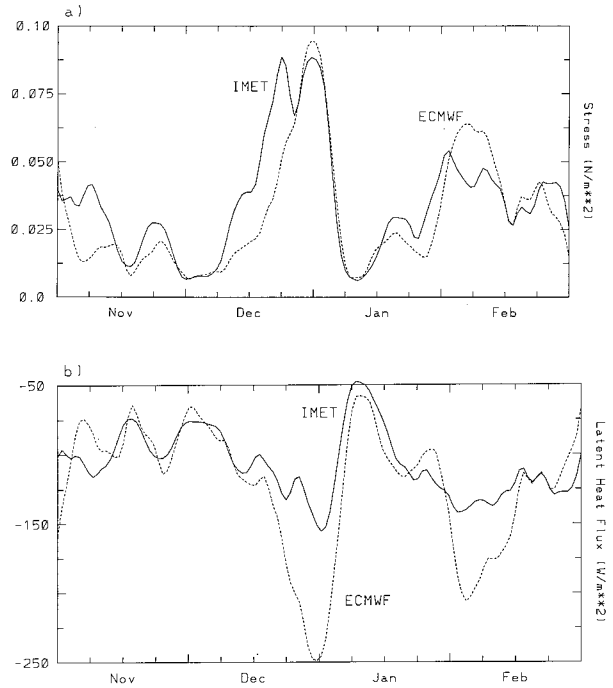


FIG. 14. Daily time series of (a) magnitude of the surface stress and (b) latent heat flux for the period 1 November 1992–28 February 1993. The solid line in each panel is the estimate from the IMET mooring at (156°E , 2°S) and the dotted line is from the estimates based on ECMWF analyses for the grid box centered at (155°E , 2.5°S). A running weekly average was applied to each time series in order to emphasize intraseasonal variations.

the stress for these times (Fig. 14a) points to an underestimation of q in the ECMWF analyses as one cause of this discrepancy. The use of a stability-independent exchange coefficient for estimation of the latent heat flux from the ECMWF analyses may also be problematic, as the difference between SST and surface air temperature was small at these times. Despite the large discrepancies during the strong wind events, the ECMWF-based estimate reasonably tracks the variability displayed in the IMET estimate. While the standard deviation of the ECMWF estimate is larger (47 vs 24 W m^{-2}), the two time series correlate at 0.79. The rms difference is 32 W m^{-2} . Thus, the estimate of latent heat flux based on the ECMWF analyses appears to qualitatively capture the intraseasonal variability observed at the IMET mooring. The amplitude of the intraseasonal variability, however, is too large due to a bias in the ECMWF-based estimates of latent heat flux during the large amplitude, post convective, westerly wind events. Whether this bias carries over to other strong westerly wind events in the 7-yr record of ECMWF analyses used here is the subject of current study.

The next issue to address with the COARE observations is the relationship between intraseasonal anomalies of organized convection and net surface insolation. Figure 15 displays time series of OLR, for the grid box centered at (155°E , 2.5°S), and the net shortwave ra-

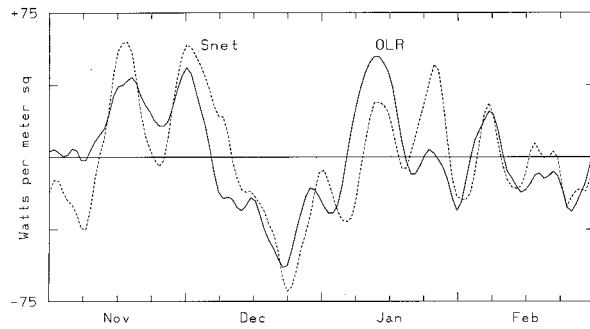


FIG. 15. Daily time series of net surface insolation (solid line) measured at the IMET mooring (156°E , 2°S) and OLR (dotted line) from the NOAA polar-orbiting satellite for the grid box centered at (155°E , 2.5°S) for the period 1 November 1992–28 February 1993. The time means for this period were removed and a weekly running average has been applied.

radiation measured at the IMET mooring. The time mean for the period 1 November 1992–28 February 1993 was removed from each series. Again, a weekly running mean was applied to each time series in order to emphasize intraseasonal timescales. The two time series correlate at 0.75, suggesting that OLR can be used as a proxy for surface insolation anomalies associated with variations in convection on intraseasonal timescales. Furthermore, the amplitude of the intraseasonal fluctuations of surface insolation and OLR are similar ($\sim 30 \text{ W m}^{-2}$), which suggests that the OLR anomalies can be used directly to approximate surface insolation anomalies. In fact, the regression coefficient based on this analysis is $0.83 (\text{W m}^{-2} \text{ shortwave}) (\text{W m}^{-2} \text{ OLR})^{-1}$.

The degree to which the surface fluxes of radiation and latent heat can account for the observed intraseasonal variations of SST is now addressed. If these surface heat fluxes were the only process affecting the temperature of the mixed layer and the SST is indicative of the temperature of the mixed layer, then the SST ought to obey

$$\frac{\partial T}{\partial t} = \frac{F_{\text{tot}}}{\rho_o C_p H}, \quad (1)$$

where T is the mean temperature of the mixed layer, F_{tot} is the total heat flux absorbed in the mixed layer (sum of latent and sensible heat flux, and net longwave and incident shortwave radiation minus the shortwave radiation, which penetrates through the base of the mixed layer), ρ_o is density of water, C_p is the specific heat of water at constant pressure, and H is the depth of the mixed layer. Following Shinoda and Lukas (1995), 60% of the incoming shortwave radiation is assumed to be absorbed at the surface. The remaining 40% is assumed to be absorbed with an e -folding scale of 20 m, which is presumed to be characteristic of the clear waters of the warm pool (Jerlov 1968). The balance in (1) assumes that the temperature is not affected by horizontal advection, nor by vertical advection and entrainment. Discounting the latter two processes for the western Pacific

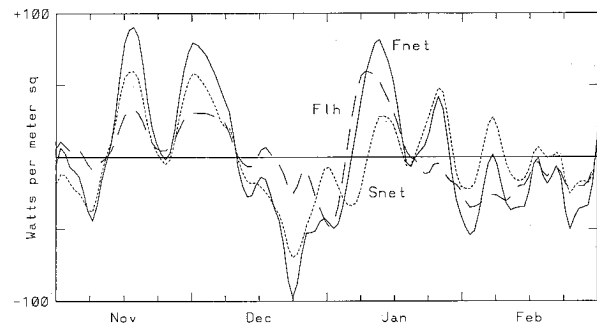


FIG. 16. Daily time series of the net surface heat flux (sum of net shortwave and longwave radiation and sensible and latent heat fluxes; solid line), net shortwave radiation at the surface (dotted line), and latent heat flux (dashed line) from the IMET mooring at (156°E , 2°S) for the period 1 November 1992–28 February 1993. The time means for this period were removed. A running weekly average was applied.

warm pool is less justifiable than the first (e.g., McPhaden and Hayes 1991).

The time series of net surface heat flux at the IMET mooring is shown in Fig. 16. Also shown are time series of latent heat flux and net shortwave radiation. A running weekly average has again been applied. The time mean of each series was removed in order to emphasize the anomalous heating and cooling episodes. The time mean net surface heat flux, latent heat flux, and shortwave radiation for this period are $+21 \text{ W m}^{-2}$, -107 W m^{-2} , and 196 W m^{-2} , respectively. The remainder of the mean net heat flux is composed of net longwave cooling (-58 W m^{-2}) and sensible heat loss (-9 W m^{-2}). Fluctuations of shortwave radiation and latent heat flux clearly dominate the intraseasonal variation of net surface heat flux. Variations of shortwave radiation are generally larger than those of latent heat flux, though the heating episode in early January is an outstanding exception. It is also apparent that the shortwave and latent heat fluxes are generally in phase. Recall that anomalous latent heat flux is observed to lag anomalous OLR by about 1 week for the canonical MJO across the western Pacific. This lack of lag here possibly may be due to the limited record of point measurements, or it may more accurately reflect the true phasing, which is not faithfully depicted in the ECMWF-based analyses. A clear lag of about 1 week between the latent heat flux and shortwave radiation does occur, however, for the strongest cooling episode during late December.

To compute the rhs of (1) requires a knowledge of the mixed-layer depth. The time series of density-based estimate of mixed-layer depth is shown in Fig. 17, along with the mean mixed-layer temperature and surface wind speed. A running weekly average was applied. The mean mixed-layer depth for COARE is estimated to be 25.5 m, which is consistent with previous estimates in the warm pool (e.g., Lukas and Lindstrom 1991). The mean, vertically averaged mixed layer temperature is 29.34°C , which is indistinguishable from the mean SST (29.36°C).

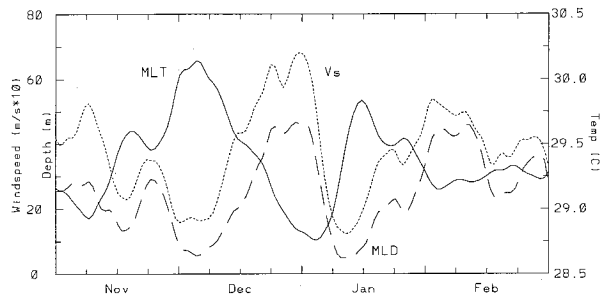


FIG. 17. Daily time series of the depth of the mixed layer (dashed line), mixed layer-mean temperature (solid line), and surface wind speed (dotted line) from the IMET mooring (156°E , 2°S) for the period 1 November 1992–28 February 1993. A running weekly average has been applied. The scale for depth is on the left ordinate (meters). The scale for wind speed is also on the left ordinate ($\text{m s}^{-1} \times 10$). The scale for the mixed layer-mean temperature is on the right ordinate ($^{\circ}\text{C}$).

The mixed layer depth varies coherently with wind speed (correlation of 0.92), which presumably reflects the role of wind forcing for deepening via entrainment (turbulent mixing) and via negative buoyancy forcing (enhanced evaporation). The mixed layer depth also varies inversely with the vertically averaged mixed layer temperature, which is also consistent with the anticipated cooling effects of these two wind-generated processes. The mixed layer temperature peaks in early December at over 30°C , drops to less than 29°C in early January and then rises again to near 30°C in mid January. One final cooling occurs in late January. These variations are seen to closely track those associated with the passage of the MJO (Fig. 13), and are thus taken as the local signature of the MJO.

Figure 18 displays the time series of the tendency of mean-mixed layer temperature (computed with centered differences using daily data) and the tendency computed from the rhs of (1). Note that the time variation of the mixed layer depth and penetration of shortwave radiation through the mixed layer were taken into account in this calculation. The observed mixed layer temperature tendency tracks that predicted from (1) reasonably well, both in amplitude and phase. The correlation between the two time series is 0.64. However, the observed tendency is seen to lead that predicted from F_{tot} by 2 days. The correlation jumps to 0.81 if this lag is accounted for. This lag could be attributed to a neglected component of the heat budget (e.g., entrainment cooling, vertical advection, or horizontal advection), which would then just be determined as the residual between the observed and computed tendencies. On the other hand, the systematic lag could indicate an error in any of the measurements.

In light of the wide intraseasonal fluctuation in mixed-layer depth, the agreement in amplitude between the predicted and observed mixed layer temperature tendency is especially significant. During the two warming episodes in late November and late December, the mixed

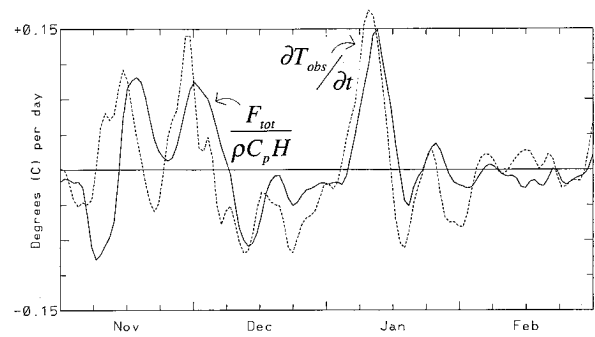


FIG. 18. Daily time series of the observed tendency of mixed layer-mean temperature at the IMET mooring (dotted line) and that predicted by the rhs of (1) using the daily fluxes and mixed layer depths from the IMET mooring (solid line) for the period 1 November 1992–28 February 1993. A weekly average was applied to both tendencies prior to plotting. The units of temperature tendency are $^{\circ}\text{C month}^{-1}$.

layer is extremely shallow (~ 10 m). These are times of weak winds, diminished evaporation, and large insolation. If the penetration of shortwave radiation through the shallow mixed layer is not accounted for (i.e., all of the shortwave radiation is prescribed to be absorbed in the mixed layer), then the predicted tendencies at these times would more than double and thus be out of line with those observed. Furthermore, the mixed layer temperature would mistakenly be predicted to increase at the rate of $\sim 2.5^{\circ}\text{C month}^{-1}$ over the course of COARE. This is in sharp contrast to the observed COARE-mean temperature tendency of $0.06^{\circ}\text{C month}^{-1}$ and predicted COARE-mean tendency (including penetrative radiation) of $0.144^{\circ}\text{C month}^{-1}$.

5. Summary and conclusions

Over the equatorial Indian and western Pacific Ocean, intraseasonal anomalies of evaporation result primarily from anomalous surface westerlies. Evaporation lags enhanced convection by about 1–2 weeks. For the MJO, the phasing between the anomalies of latent heat flux and convection varies over its life cycle: Latent heat flux anomalies shift from lagging anomalous OLR by about 2 weeks across the Indian Ocean to less than 1 week across the western Pacific. This change in phasing is consistent with the evolution of surface zonal wind over the life cycle of the MJO shown by Hendon and Salby (1994). They show the convective anomaly, when it is developing over the Indian Ocean, to be near the node of the anomalous surface zonal wind. This phasing is consistent with anomalous evaporation occurring 1/4 cycle later in the region of maximum anomalous westerlies. Over the western Pacific, Hendon and Salby (1994) show anomalous surface westerlies (and, hence, evaporation) lag anomalous convection by less than 1 week.

Zhang (1996) finds, on the other hand, that anomalous evaporation slightly *leads* anomalous convection over the western Pacific. As Zhang (1996) used direct ob-

servations from buoys, it is worth commenting on possible reasons for the discrepancy with the phasing found here based on ECMWF analyses. Clearly, errors (systematic and otherwise) exist in the ECMWF analyses. However, the limited comparison with observations at the IMET mooring suggests that at least the gross characteristics of the intraseasonal behavior are captured in the ECMWF analyses. On the other hand, in order to create a useful record length, Zhang (1996) had to average time series from individual buoys over a large domain (8°N–8°S, 147°–170°E). Zhang comments that the buoy data are biased toward the eastern portion of the domain, which may introduce systematic errors when the phase between these averaged surface fields and evenly sampled fields such as satellite-based cloudiness are computed. Resolution of this discrepancy for the phasing of evaporation and convective anomalies is required, as their phasing bears on the role that anomalous evaporation plays in driving the MJO.

That enhanced evaporation lags enhanced convection throughout the entire life cycle of the MJO, as found here using ECMWF analyses, would appear to be at odds with linear theories of evaporation-wind feedback (e.g., Emanuel 1987), which predict feedback for a Kelvin-like mode when anomalous evaporation leads anomalous convection. The picture presented in Fig. 9 is very much different than that for the MJO in a global model shown by Neelin (1988), for which he attributes evaporation-wind feedback to be playing a significant role. In his model composite, evaporative anomalies *are not* found to the west of the convective anomalies while the convection is in the Indian Ocean. In fact, minimal evaporative anomalies are found over the entire Indian and far western Pacific Ocean. On the other hand, Neelin finds large evaporative anomalies over the central Pacific, in advance of the convective anomaly. These evaporative anomalies result from enhanced easterlies in regions of mean easterlies. The phasing of these evaporative anomalies in the model is consistent with that required for evaporative-wind feedback for an eastward-propagating Kelvin-like disturbance. Neelin rightly argues that the large-scale nature of the MJO does not necessarily require evaporative-wind feedback over the Indian Ocean, as long as it is occurring elsewhere, in order for the mechanism to work. Furthermore, as pointed out by Emanuel (1988), drawing conclusions based on local correlations is tenuous considering the planetary-scale structure of the MJO. However, it is difficult to reconcile their arguments with the observed behavior found here. Large evaporative anomalies are observed only west of about 160°W, in regions of weak mean westerlies, and only west of the convective anomalies. These evaporative anomalies do not appear to feedback in support of an eastward propagating Kelvin-like mode. The only evaporative anomalies that possibly may be doing so, at least in the context of the simple theory of evaporation-wind feedback, are the minuscule ones found in the far eastern Pacific. That these weak evap-

orative anomalies are driving the MJO is difficult to believe.

On the other hand, the role of frictionally driven convergence for promoting convection, which can fuel the large-scale circulation anomaly (e.g., Wang and Rui 1990; Salby et al. 1994), appears to be supported by the present findings. Enhanced surface humidity was shown to occur in phase with surface low pressure and to lead anomalous convection, though by a varying amount, over the entire life cycle of the MJO. Hendon and Salby (1994) showed that surface convergence, which presumably exerts strong control of the surface humidity, is primarily frictionally controlled, with cross-isobaric flow occurring into the surface low. They further showed that the convective anomaly is nearly in-phase with surface convergence (and enhanced surface humidity; e.g., Fig. 11) while it is developing over the Indian Ocean. In this configuration, anomalous convection is more in-phase with anomalous tropospheric-mean temperature (and surface low pressure), and hence eddy available energy is generated and converted to kinetic energy. When the convective anomaly is decaying over the western Pacific, more of a lag (1/4 cycle) with temperature, surface low pressure, and surface humidity (Fig. 12) is found. In this configuration, frictional surface convergence into the surface low, which is now well to the east of the main convective anomaly (Hendon and Salby 1994), occurs over colder waters of the central and eastern Pacific. Here, it is not as effective for promoting enhanced surface humidity and, hence, convection which could fuel the anomalous large-scale circulation.

Spatially coherent SST anomalies propagate eastward across the Indian and western Pacific Ocean in conjunction with the MJO. Typical amplitudes are 1/4° to 1/3°C. Exceptionally large events, such as occurred during TOGA COARE, may produce swings in SST greater than 1°C. The potential impact of these SST anomalies is highlighted by noting that, at 30°C, a 1°C swing in SST is associated with a 1.74 g kg⁻¹ change in saturation mixing ratio or about a 7°C change in saturation equivalent potential temperature. Whether these anomalies indeed influence convection over the warm pool and, in particular, whether they play an active role in the MJO is the subject of ongoing studies.

These SST anomalies are postulated to be driven predominantly by surface insolation anomalies, generated by anomalous large-scale convection, and by anomalous latent heat flux, associated with regions of anomalous windspeed. The insolation anomalies have typical magnitudes of 25–30 W m⁻², while the latent heat flux anomalies are slightly weaker (20–25 W m⁻²). A limited comparison of the fluxes based on ECMWF analyses with those estimated at the IMET mooring during COARE, however, suggests that the amplitude of the intraseasonal latent heat flux anomalies may be overestimated from the ECMWF-based analysis.

Warm SST is observed to occur about 1/4 cycle (~2

weeks) after suppressed convection throughout the Indian and western Pacific Oceans. On the other hand, reduced evaporation is nearly in-phase with the SST anomalies in the Indian Ocean but evolves to near quadrature over the western Pacific. The relative role of the insolation anomalies for driving SST changes appears to be greater in the Indian Ocean than in the western Pacific, as indicated by the relatively smaller amplitude of the latent heat flux anomalies and their more nearly in-phase relationship with the SST anomalies in the Indian Ocean.

SST in the Indian and western Pacific warm pool is sensitive to these intraseasonal surface heat flux anomalies because the mean mixed-layer depth is only ~ 25 m. This shallow mixed layer results from stratification provided by the enormous freshwater flux into these regions (e.g., Lukas and Lindstrom 1991). However, the depth of the mixed layer is observed to vary systematically over the life cycle of the MJO. The shallowest mixed layer (~ 10 m) occurs during the calmest and sunniest conditions, when the heat flux into the ocean is large and little turbulent entrainment is generated by the wind. The deepest mixed layer (~ 50 m) occurs during the windiest and cloudiest conditions when the heat flux into the ocean is small (even negative) and turbulent mixing is large.

This variation in mixed layer depth has important consequences for the sensitivity of the mixed layer temperature (and SST) to the surface heat flux anomalies. On the one hand, the shallow mixed layer during the sunny/calm phase will tend to increase the sensitivity to the positive heat flux anomalies at this time due to a decreased heat capacity. On the other hand, during the cloudy/windy phase the sensitivity to the negative heat flux anomalies is reduced due to a larger heat capacity (deeper mixed layer). The sensitivity during the sunny/calm phase is also reduced due to the significant amount of shortwave radiation, which penetrates through the mixed layer when it is at its shallowest. This shortwave radiation that penetrates through the shallow mixed layer may then directly warm the sub-mixed layer (though static stability is maintained due to the freshness of the mixed layer). This heat may be reintroduced into the mixed layer when it subsequently deepens during the windy/cloudy phase. This effect will thus further act to reduce the amplitude of intraseasonal SST perturbations driven by the surface heat fluxes associated with the MJO.

It is also interesting to note that a near-zero mean tendency of mixed layer temperature is observed at the IMET mooring during COARE even in the presence of a net surface heat flux of roughly 20 W m^{-2} . If this 20 W m^{-2} were totally absorbed in a mixed layer of mean depth 25 m, then a warming at the rate of $0.5^\circ\text{C month}^{-1}$ would occur. The observed tendency during COARE was $0.06^\circ\text{C month}^{-1}$ and that estimated from the IMET surface fluxes, taking into account the intraseasonally varying mixed-layer depth and penetration of shortwave

radiation, is $0.14^\circ\text{C month}^{-1}$. Thus, without evoking any ocean dynamics, a reasonably constant mixed layer temperature is maintained in the presence of $\sim 20 \text{ W m}^{-2}$ net heat flux. However, the issue of what happens to shortwave radiation that penetrates below the intraseasonally varying mixed layer is not addressed in this simple diagnostic analysis and, thus, requires further study.

Acknowledgments. Bob Weller kindly provided the observations from the WHOI IMET mooring. Toshi Shinoda generated the time series of mixed-layer depth from the IMET data. Insightful comments by the two anonymous reviewers led to substantial improvements in the manuscript. This work was supported by a TOGA COARE grant from NOAA's Office of Global Programs.

REFERENCES

- Blackman, R., and J. Tukey, 1959: *The Measurement of Power Spectra*. Dover, 190 pp.
- Emanuel, K. A., 1987: An air-sea interaction model of the intraseasonal oscillation in the tropics. *J. Atmos. Sci.*, **44**, 2324–2340.
- , 1988: Reply. *J. Atmos. Sci.*, **45**, 3528–3530.
- Fairall, C., E. F. Bradley, D. P. Rogers, J. B. Edson, and G. S. Young, 1996: The TOGA COARE bulk flux algorithm. *J. Geophys. Res.*, **101**, 3747–3764.
- Gruber, A., and A. F. Krueger, 1984: The status of the NOAA outgoing longwave radiation data set. *Bull. Amer. Meteor. Soc.*, **65**, 958–962.
- Gutzler, D. S., G. N. Kiladis, G. A. Meehl, K. M. Weickmann, and M. Wheeler, 1994: The global climate of December 1992–February 1993. Part II: Large-scale variability across the tropical western Pacific during TOGA COARE. *J. Climate*, **7**, 1606–1622.
- Harrison, D. E., and P. S. Schopf, 1984: Kelvin-wave-induced anomalous advection and the onset of surface warming in El Niño events. *Mon. Wea. Rev.*, **112**, 923–933.
- Hendon, H. H., and M. L. Salby, 1994: The life cycle of the Madden-Julian oscillation. *J. Atmos. Sci.*, **51**, 2225–2237.
- , and —, 1996: Planetary-scale circulations forced by intraseasonal variations of observed convection. *J. Atmos. Sci.*, **53**, 1751–1758.
- Hsu, H.-H., B. J. Hoskins, and F.-F. Jin, 1990: The 1985/86 intraseasonal oscillation and the role of the extratropics. *J. Atmos. Sci.*, **47**, 823–839.
- Jerlov, N. G., 1968: *Optical Oceanography*. Elsevier, 194 pp.
- Johnson, E. S., and M. J. McPhaden, 1993: Structure of intraseasonal Kelvin waves in the equatorial Pacific Ocean. *J. Phys. Oceanogr.*, **23**, 608–625.
- Kessler, W. S., M. J. McPhaden, and K. M. Weickmann, 1995: Forcing of intraseasonal Kelvin waves in the equatorial Pacific. *J. Geophys. Res.*, **100**, 10 613–10 631.
- Knutson, T. R., and K. M. Weickmann, 1987: 30–60 day atmospheric oscillations: Composite life cycles of convection and circulation anomalies. *Mon. Wea. Rev.*, **115**, 1407–1436.
- Krishnamurti, T. N., D. K. Osterhof, and A. V. Mehta, 1988: Air-sea interaction on the time scale of 30 to 50 days. *J. Atmos. Sci.*, **45**, 1304–1322.
- Lau, K. M., and P. H. Chan, 1985: Aspects of the 40–50 day oscillation during the northern winter as inferred from outgoing longwave radiation. *Mon. Wea. Rev.*, **113**, 1889–1909.
- Lukas, R., and E. Lindstrom, 1991: The mixed layer of the western equatorial Pacific Ocean. *J. Geophys. Res.*, **96**, 3343–3357.
- Madden, R. A., and P. Julian, 1972: Description of global-scale cir-

- ulation cells in the tropics with 40–50 day period. *J. Atmos. Sci.*, **29**, 1109–1123.
- McPhaden, M. J., and S. P. Hayes, 1991: On the variability of winds, sea surface temperature, and surface layer heat content in the western equatorial Pacific. *J. Geophys. Res.*, **96**, 3331–3342.
- Murakami, T., L.-X. Chen, A. Xie, and M. L. Shrestha, 1986: Eastward propagation of 30–60 day perturbations as revealed from outgoing longwave radiation data. *J. Atmos. Sci.*, **43**, 961–971.
- Neelin, J. D., 1988: Reply. *J. Atmos. Sci.*, **45**, 3526–3527.
- North, G. R., T. L. Bell, R. F. Cahalan, and F. J. Moeng, 1982: Sampling errors in the estimation of empirical orthogonal functions. *Mon. Wea. Rev.*, **110**, 699–706.
- Panofsky, H. A., and G. W. Brier, 1968: *Some Applications of Statistics to Meteorology*. The Pennsylvania State University, 224 pp.
- Reynolds, R. W., and T. M. Smith, 1994: Improved global sea surface temperature analyses using optimum interpolation. *J. Climate*, **7**, 929–948.
- Salby, M. L., and H. H. Hendon, 1994: Intraseasonal behavior of clouds, temperature, and motion in the Tropics. *J. Atmos. Sci.*, **51**, 2207–2224.
- , R. R. Garcia, and H. H. Hendon, 1994: Planetary-scale circulations in the presence of climatological and wave-induced heating. *J. Atmos. Sci.*, **51**, 2344–2367.
- Shinoda, T., and R. Lukas, 1995: Lagrangian mixed layer modeling of the western equatorial Pacific. *J. Geophys. Res.*, **100**, 2523–2541.
- Wang, B., and H. Rui, 1990: Dynamics of the coupled moist Kelvin–Rossby wave on an equatorial β plane. *J. Atmos. Sci.*, **47**, 397–413.
- Webster, P. J., 1994: The role of hydrological processes in ocean–atmosphere interactions. *Rev. Geophys.*, **32**, 427–476.
- , and R. Lukas, 1992: TOGA COARE: The Coupled Ocean–Atmosphere Response Experiment. *Bull. Amer. Meteor. Soc.*, **73**, 1377–1417.
- Weickmann, K., 1983: Intraseasonal circulation and outgoing longwave radiation modes during northern winter. *Mon. Wea. Rev.*, **111**, 1838–1858.
- Weller, R. A., and S. P. Anderson, 1996: Surface meteorology and air–sea fluxes in the western equatorial Pacific warm pool during the TOGA Coupled Ocean–Atmosphere Response Experiment. *J. Climate*, **9**, 1959–1990.
- Zhang, C., 1996: Atmospheric intraseasonal variability at the surface in the tropical western Pacific Ocean. *J. Atmos. Sci.*, **53**, 739–758.
- , and M. J. McPhaden, 1995: The relationship between sea surface temperature and latent heat flux in the equatorial Pacific. *J. Climate*, **8**, 589–605.